Nano Research 2018, 11(5): 2821–2835
https://doi.org/10.1007/s12274-017-1912-9
Research Article
ISSN 1998-0124
CN 11-5974/O4

Highly efficient catalytic scavenging of oxygen free radicals with graphene-encapsulated metal nanoshields

Junying Wang[1,§], Xiaoju Cui[2,3,4,§], Haobo Li[2,4,§], Jianping Xiao[2], Jiang Yang[6], Xiaoyu Mu[1], Haixia Liu[1], Yuan-Ming Sun[5], Xuhui Xue[5], Changlong Liu[1], Xiao-Dong Zhang[1] (✉), Dehui Deng[2,3] (✉), and Xinhe Bao[2]

[1] *Department of Physics, Tianjin Key Laboratory of Low Dimensional Materials Physics and Preparing Technology, School of Science, Tianjin University, Tianjin 300350, China*
[2] *State Key Laboratory of Catalysis, Collaborative Innovation Center of Chemistry for Energy Materials, Dalian Institute of Chemical Physics, Chinese Academy of Sciences, Dalian 116023, China*
[3] *State Key Laboratory for Physical Chemistry of Solid Surfaces, Collaborative Innovation Center of Chemistry for Energy Materials, College of Chemistry and Chemical Engineering, Xiamen University, Xiamen 361005, China*
[4] *University of Chinese Academy of Sciences, Beijing 100039, China*
[5] *Tianjin Key Laboratory of Molecular Nuclear Medicine, Institute of Radiation Medicine, Chinese Academy of Medical Sciences and Peking Union Medical College, Tianjin 300192, China*
[6] *State Key Laboratory of Oncology in South China, Collaborative Innovation Center for Cancer Medicine, Sun Yat-sen University Cancer Center, Guangzhou 510060, China*
[§] *Junying Wang, Xiaoju Cui, and Haobo Li contributed equally to this work.*

Received: 3 October 2017
Revised: 25 October 2017
Accepted: 4 November 2017

KEYWORDS
biocatalytic processes, radiation protection, graphene-encapsulated metal nanoparticles, oxygen free radical, DFT calculations

ABSTRACT

Normal levels of oxygen free radicals play an important role in cellular signal transduction, redox homeostasis, regulatory pathways, and metabolic processes. However, radiolysis of water induced by high-energy radiation can produce excessive amounts of exogenous oxygen free radicals, which cause severe oxidative damages to all cellular components, disrupt cellular structures and signaling pathways, and eventually lead to death. Herein, we show that hybrid nanoshields based on single-layer graphene encapsulating metal nanoparticles exhibit high catalytic activity in scavenging oxygen superoxide ($\cdot O_2^-$), hydroxyl ($\cdot OH$), and hydroperoxyl ($HO_2\cdot$) free radicals via electron transfer between the single-layer graphene and the metal core, thus achieving biocatalytic scavenging both *in vitro* and *in vivo*. The levels of the superoxide enzyme, DNA, and reactive oxygen species measured *in vivo* clearly show that the nanoshields can efficiently eliminate harmful oxygen free radicals at the cellular level, both in organs and circulating blood. Moreover, the nanoshields lead to an increase in the overall survival rate of gamma ray-irradiated mice to up to 90%, showing the great potential of these systems as protective agents against ionizing radiation.

Address correspondence to Xiao-Dong Zhang, xiaodongzhang@tju.edu.cn; Dehui Deng, dhdeng@dicp.ac.cn

1 Introduction

Ionizing radiation plays an important role in medical diagnosis and therapy. However, in addition to its obvious benefits, it also presents potential health risks [1, 2]. High-energy ionizing radiation (X- and gamma-rays) used in radiotherapy not only kills cancer cells, reduces tumor malignancies, and relieves cancer symptoms, but also inevitably causes severe damages to healthy tissues and organs [3, 4]. The high-energy radiation induces ionization of water through radiolysis and generates excessive levels of exogenous reactive oxygen species (ROS), such as superoxide ($\cdot O_2^-$) and hydroxyl ($\cdot OH$) radicals, through photoelectric, Compton scattering, and Auger effects [5]. Excessive ROS levels damage all cellular components, from nucleic acid and lipids to proteins, and lead to DNA double-strand breaks, oxidative stress, as well as adverse chemical and biological events at the molecular and cellular level, eventually causing malfunction [6–8], and failure of the entire biosystem [9]. Radioprotective agents provide a feasible solution to minimize adverse effects and improve the efficacy of radiotherapy [10–17], and especially of high-dose treatments. Amifostine (Ethyol®) and 3,3′-diindolylmethane (DIM) have been employed as clinical adjuvants to protect healthy tissues by removing radiation-induced free radicals, but their short blood elimination half-life (< 10 min) largely hinders a sustained scavenging activity against oxygen free radicals [11]. Previous studies showed that CeO_2 nanoparticles with high vacancy contents can prolong the circulation time of the radioprotective agents and improve the overall survival rate of mice [17, 18]. However, these organic and inorganic radioprotective agents usually result in suboptimal survival rates of irradiated mice. Radiation protection essentially involves biocatalytic processes to scavenge ROS at single-molecular, cellular, and whole-body levels [19, 20]. Therefore, it is highly desirable to design a new family of materials with high catalytic activity in the elimination of free radicals, which could be employed as adjuvants to increase survival rates in radio- and/or chemotherapy.

It has been previously demonstrated that graphene-encapsulated metal nanohybrids possess outstanding catalytic activity towards the oxygen reduction reaction (ORR) and oxygen evolution reaction (OER) processes, enabling the conversion of adsorbed OH and O species to H_2O and O_2 [21–25], and providing a route to scavenge oxygen free radicals. Herein, we prepared a family of highly active single-layer graphene-encapsulated metal nanohybrids (M@Cs) to study their *in vivo* biocatalytic activity and radioprotective effects, as well as the underlying mechanism of their activity against free radicals. Electrochemical characterizations and density functional theory (DFT) calculations, used to model the scavenging of oxygen free radicals, highlighted the extraordinary electrocatalytic activity of the M@Cs in the reduction of oxygen, hydrogen peroxide, and ozone, via a unique electronic transfer mechanism between the one atom-thick graphene layer and the metal core. The as-prepared hybrid nanoshields, consisting of graphene-encapsulated metal nanoparticles (NPs), can effectively eliminate free radicals from major organs through reduction reactions. In addition, superoxide dismutase (SOD), an important indicator of the antioxidant capacity in almost all living cells exposed to oxygen, significantly recovered back to the initial normal level, highlighting the repair capabilities of the nanoshields against radiation-induced damages. As a result, graphene-encapsulated Fe and CoNi nanoshields (Fe@C and CoNi@C) improved the surviving rate of mice exposed to high-energy radiation (662 keV) to values as high as 90% and 80%, respectively. These rates are higher than those achieved with all other available radioprotectants, including the clinically effective amifostine (Ethyol®). The systematic *in vivo* pharmacokinetic and toxicological profiles of Fe@C and CoNi@C did not reveal any appreciable toxicological effects for more than 30 days post-injection.

2 Results and discussion

M@Cs were synthesized according to the procedure reported in our previous work [22]. High-resolution transmission electron microscopy (HRTEM) was employed to inspect the morphology of the M@Cs. As shown in Fig. 1(a), metal NPs of 6–10 nm are uniformly distributed on interconnected carbon nanotubes. Further analysis (Figs. 1(b) and 1(c)) indicates that

the metal NP cores were completely encapsulated by a graphene layer of approximately 3.4 Å. A *d* spacing of 2.0 and 2.1 Å was measured for Fe@C and CoNi@C, respectively, in good agreement with the (110) and (111) interplanar distances of the metallic Fe and CoNi alloy, respectively.

A conventional three-electrode electrochemical cell was used to evaluate the electrocatalytic activities of M@Cs in the reduction of oxygen, hydrogen peroxide, and ozone, which involve the conversion of ·OH, HO_2·, and $\cdot O_2^-$ species. As shown in Fig. 1(d), rotating disk electrode (RDE) measurements showed strong ORR performances for all M@Cs, with Fe@C and CoNi@C exhibiting the highest catalytic activities. The best catalytic performance for the H_2O_2 reduction was observed for FeNi@C, followed by Fe@C (Fig. 1(e)). Also Fe@C exhibited the highest catalytic activity in the O_3 reduction (Fig. 1(f)). The cyclic voltammograms (CVs) of Fe@C and CoNi@C (Figs. 1(g)–1(i)) show a sharp increase in reduction current density in the presence of O_2, H_2O_2, and O_3 as the potential scan is shifted to values lower than 0.6 V. However, only a negligible reduction current density was observed for an unmodified glassy carbon electrode (GCE), highlighting the extraordinary catalytic activity of Fe@C and CoNi@C toward the above reduction reactions. In addition, the reduction activity of graphite and graphene nanosheets was also evaluated (Figs. S1 and S2 in the Electronic Supplementary Material, ESM), and found to be significantly lower than that of the M@Cs. The high catalytic activity of the M@Cs in the reduction of O_2, H_2O_2, and O_3 results in the efficient conversion of oxygen free radicals to O_2 and H_2O. The catalytic processes were simulated using density functional theory (DFT) calculations, as discussed below.

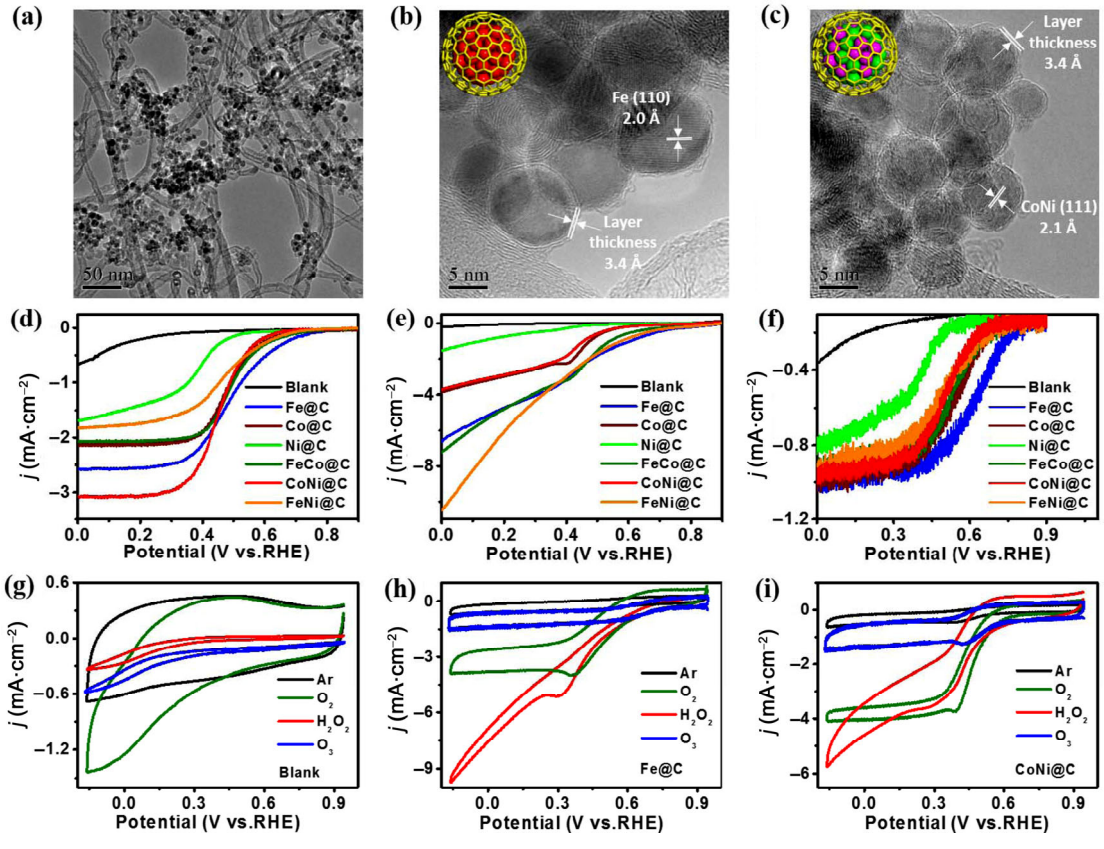

Figure 1 Morphological and electrochemical characterization of M@Cs. (a) TEM image of Fe@C, showing metal NPs distributed within the carbon nanotube network. (b) and (c) HRTEM images of Fe@C and CoNi@C, with lattice spacings outlined. The insets display schematic illustrations the structure of Fe@C and CoNi@C. (d)–(f) Linear sweep voltammetry (LSV) plots of GCE modified with M@Cs in O_2-saturated (d), 10.0 mM H_2O_2 (e), and O_3-saturated 0.1 M phosphate-buffered saline (PBS) at pH 7.4 (f). Scan rate: 5 mV·s^{-1}. (g)–(i) CVs of unmodified GCE (blank) and GCE modified with Fe@C and CoNi@C in Ar-saturated, O_2-saturated, Ar-saturated 10.0 mM H_2O_2 solution, and O_3-saturated 0.1 M PBS at pH 7.4. Scan rate: 50 mV·s^{-1}.

The reduction of oxygen free radicals on the surface of the M@Cs was investigated by quantum chemical calculations of metal clusters bonded to single-layer graphene (Fig. 2(a)). Following adsorption of ·OH radicals onto the graphene layer, the adsorbed *OH species combine with a proton to form H_2O (Process 1). Surface-adsorbed $\cdot O_2^-$ radicals desorb in the form of O_2 by transferring an electron to the surface (Process 2). This mechanism applies to FeNi@C and CoNi@C, as O_2 tends to desorb in these cases (see Table S1 in the ESM). While O_2 preferentially adsorbs on the surface of Fe@C, Co@C, and FeCo@C, the adsorbed $*O_2$ is reduced to H_2O via the ORR process (Process 3). ·OOH and ·O radicals adsorb on the surface and form *OOH and *O, respectively, both of which are then converted to H_2O (Process 3).

The primary step of the ORR on the surface of carbon-based catalysts is generally considered to be an associative process [26], involving O_2 as initial state, *OOH, *O, and *OH as intermediate states, and H_2O as final state. The binding energy of the *OH (ΔE_{OH}) and *O (ΔE_O) species is a good descriptor of the ORR activity. A good catalyst must have medium ΔE_O and ΔE_{OH} values (not too high or too low) to balance the reaction barriers in the adsorption and desorption steps [27, 28]. The ORR activity is plotted as a function of ΔE_O and ΔE_{OH} in Fig. 2(b). The theoretical derivation of ORR activities of the catalysts synthesized in this work (white dots) are close to the theoretical maximum values (red regions), where Fe@C and CoNi@C have higher activities than other structures. Since the rate-determining steps of the ORR process are generally considered to be the formation of *OOH ($O_2 \rightarrow$ *OOH) and H_2O (*OH $\rightarrow H_2O$) [27], the reduction reactions of the radicals (Processes 1 and 3) can be described by the same ORR processes. The quantum chemical calculations provide atomic-level insights into the scavenging processes.

The superior electrocatalytic activities of the present systems inspired us to further investigate their *in vitro* and *in vivo* biocatalytic performances and radioprotective effects. We evaluated the *in vitro* cellular toxicities of Fe@C and CoNi@C (Figs. S3(a) and S3(b) in the ESM), and no statistically significant toxicity was detected after 24 and 48 h of incubation, proving the low toxicities of these systems, consistent with previous work [29–32]. The SOD and glutathione (GSH) levels were tested on two cell lines, Chinese hamster ovary (CHO)-K1 and H460, with or without treatment with M@Cs. The results in Figs. S4(a) and S4(b) in the ESM indicate that both cell lines showed no statistical differences between control and M@Cs

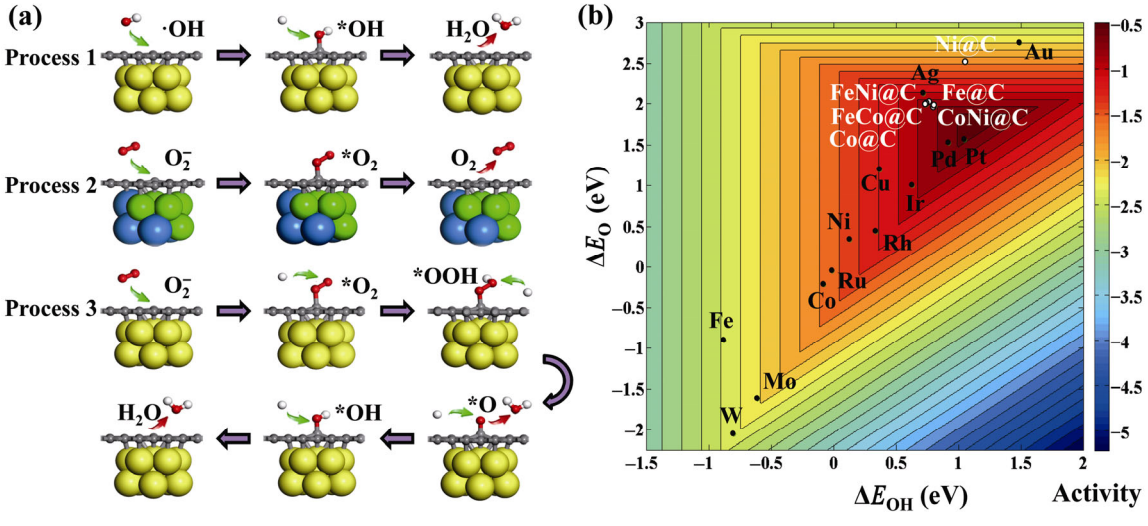

Figure 2 (a) Scavenging of oxygen free radicals on the surface of M@Cs simulated by DFT calculations. Process 1: ·OH conversion to H_2O. Process 2: $\cdot O_2^-$ conversion to O_2. Process 3: $\cdot O_2^-$ conversion to H_2O. Green arrows denote adsorption or reactive steps, and red arrows indicate desorption steps. C, O, and H atoms are represented as grey, red, and white spheres, respectively, whereas yellow, blue, and green spheres represent metal atoms. (b) Plots of oxygen reduction activities vs. *O and *OH binding energies. Red to blue colors mark oxgen reduction activities changing from high to low. The corresponding positions located by ΔE_O and ΔE_{OH} values of M@Cs (Fe, Co, Ni, and alloys) are plotted as white dots. Black dots denote data obtained from Ref. [26].

treated groups. The Fe@C and CoNi@C hybrids show increasing cellular uptake with increasing incubation time (Fig. S5 in the ESM). To evaluate the scavenging activities, Figs. 3(a)–3(d) show the intracellular ROS levels of CHO cells for the control group and for the groups subjected to irradiation only and to both irradiation and treatment with Fe@C or CoNi@C. The control group showed low ROS counts, while irradiation resulted in significant intracellular ROS levels. Pretreatment with Fe@C and CoNi@C achieved significant cellular recovery and minimized the harmful effects of the radiation (Fig. 3(i)), suggesting an important role of the treatments in removing ROS. To quantitatively determine DNA damages, single-cell gel electrophoresis was employed to estimate the DNA tail moment (Figs. 3(e)–3(h)). Radiation induced a distinct tail, corresponding to significant DNA damages. In contrast, cells treated with Fe@C and CoNi@C after irradiation showed insignificant tails and negligible DNA damages, which confirms that Fe@C and CoNi@C help in reducing and repairing radiation-induced DNA damage. The latter damage was analyzed by measuring the tail DNA and tail moment, which are the two most common parameters used for this purpose. The percent of tail DNA is defined as (tail DNA intensity/cell DNA intensity) × 100, whereas the tail moment is calculated as tail DNA (%) × tail length. These two indicators represent the damage intensity, the extent of DNA migration, and the content of tail DNA. Quantitative analysis (Figs. 3(j)–3(k)) confirmed that irradiated CHO cells treated with Fe@C and CoNi@C presented a tail moment of 0.58–0.65, significantly lower than the value of 1.46 measured after radiation exposure.

The *in vitro* protection against ionizing radiation provided by Fe@C and CoNi@C was further investigated

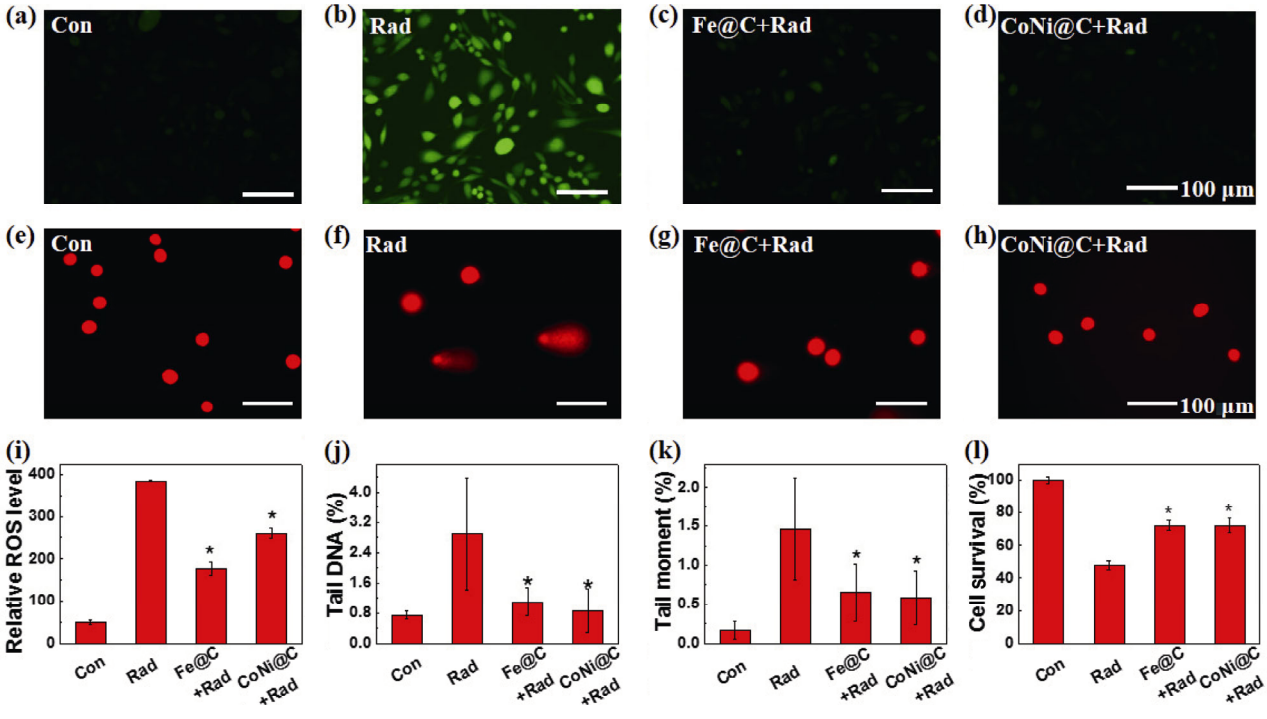

Figure 3 *In vitro* radioprotective characterization of M@Cs. (a)–(d) Fluorescence microscopy images showing ROS levels in CHO cells without irradiation, with 3 Gy gamma irradiation, and with Fe@C and CoNi@C treatments before irradiation. The cellular ROS levels are much higher in the cells exposed to radiation compared with the other groups, demonstrating the excellent radioprotective effects of the treatments, achieved by scavenging excess ROS. The corresponding quantitative data are presented in panel (i). Significant differences were found between the group exposed to radiation alone and the groups exposed to radiation and pretreated with Fe@C and CoNi@C (* indicates $p < 0.01$). (e)–(h) Comet assay showing significant tail moment values only in the group exposed to radiation, while the cells in the other groups exhibited normal morphologies. The quantification of tail DNA percentage and tail moment (j) and (k) revealed a significant reduction in radiation-induced DNA damages in the groups treated with Fe@C and CoNi@C (* indicates $p < 0.01$). (l) Survival rates of CHO cells after exposure to 3 Gy gamma radiation. Significant differences were found between cells only exposed to radiation (~ 48 %) and cells exposed to radiation with the pretreatment of Fe@C and CoNi@C (~ 72 %) (* indicates $p < 0.01$).

at the cellular level (Fig. 3(l)). The number of survived cells following irradiation and treatment with Fe@C and CoNi@C is close to healthy levels and significantly higher than that after irradiation, indicating the significant radioprotective effects of the treatments. We also tested the *in vitro* radiation protection of the M@Cs using standard colony forming assays (Fig. S6 in the ESM) [33], with results similar to those of the neutral red (NR) assay in Figs. 3(i)–3(l). The *in vitro* radiation protection of M@Cs on cancer cells (Hela and H460) was also assessed (Fig. S7 in the ESM), and the results show that healthy cells (CHO) are more sensitive to Fe@C and CoNi@C treatments than the Hela and H460 cancer cells. These findings clearly highlight the cellular selectivity of the M@Cs, which is based on the different DNA structure of healthy and cancer cells [13], and may be beneficial for the radioprotective effects of these systems.

The *in vivo* radiation shielding effects of the M@Cs (M = Fe, Ni, Co, FeCo, FeNi, and CoNi) nanohybrids was tested on C57BL/6 mice over 30 days (Fig. 4(a) and Figs. S8(a) and S8(b) in the ESM). All M@Cs showed significant protection against gamma rays, and their corresponding survival rates showed a positive correlation with the electrocatalytic performance. Healthy mice presented a survival rate of 100%, whereas the survival rate of irradiated mice sharply decreased to 10%. Irradiated mice treated with amifostine showed 80% survival rate. In contrast, irradiated mice treated with Fe@C and CoNi@C showed highest survival rates of 90% and 80%, respectively, consistent with the electrocatalytic and DFT results, demonstrating the excellent systemic protection of the nanoshields against radiation. Notably, graphene nanosheets and graphite yielded survival rates of only ~ 10% (Fig. S8(b) in the ESM),

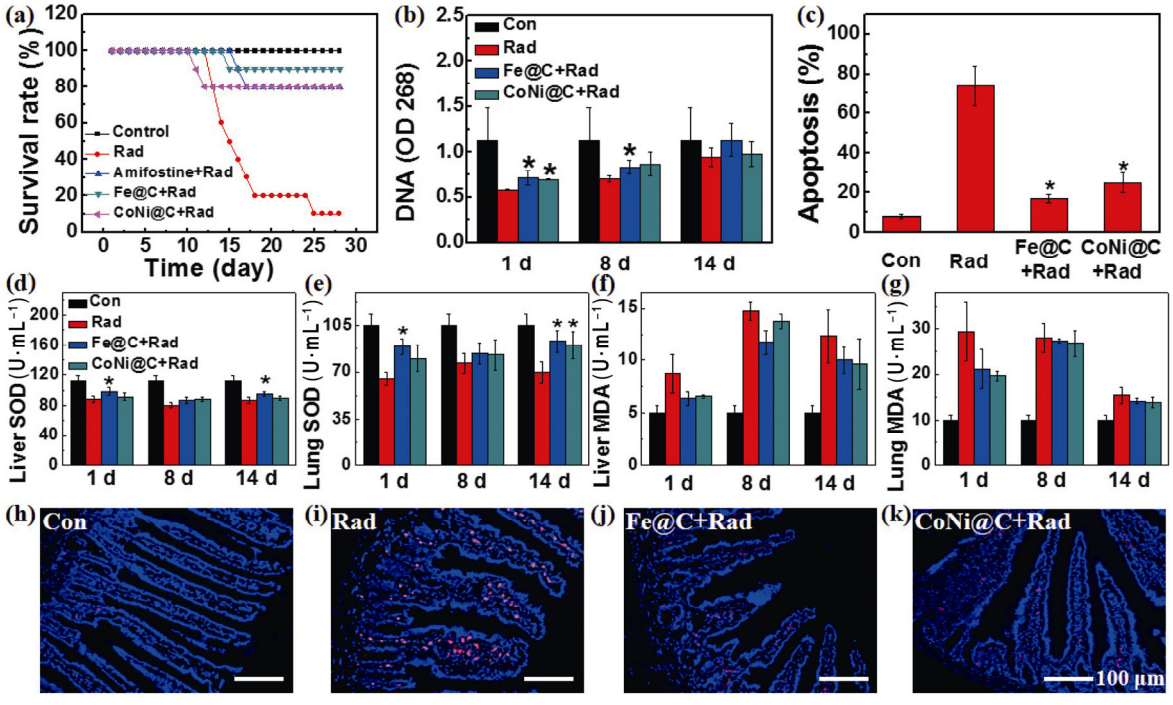

Figure 4 *In vivo* radioprotective characterization of M@Cs. (a) Survival rates of healthy mice, irradiated mice, and mice irradiated pretreated with amifostine, Fe@C, and CoNi@C. During the observation period of 30 days, the survival rates of mice in control, irradiated only, Fe@C-treated, and CoNi@C-treated groups were 100%, 10%, 90%, and 80% respectively. (b) Total DNA of bone marrow after 1, 8, and 14 days for control, irradiated only, Fe@C-, and CoNi@C-treated groups, showing the recovery process after irradiation. The amount of total DNA in mice treated with Fe@C and CoNi@C showed a significant increase compared to that in irradiated-only mice ($p < 0.05$) after 1 and 14 days. (c) Cell apoptosis determined by measuring red apoptotic fluorescence signals (h)–(k) in intestine tissue sections after 13 Gy abdominal irradiation. (d)–(g) Oxidative stress and antioxidant defense levels measured 1, 8, and 14 days after irradiation. The SOD levels in liver and lung increased dramatically after treatment compared to the levels after irradiation ($p < 0.05$), while lower MDA levels were measured after treatment with Fe@C and CoNi@C compared to the levels after irradiation, demonstrating the efficient radiation shielding of Fe@C and CoNi@C.

confirming that the protection effects of the present systems originate from their intrinsic catalytic activities, rather than from graphene itself. Similar trends were observed for the body weight after 7.5 Gy radiation (Fig. S8(a) in the ESM). The total DNA in bone marrow and the number of bone marrow nucleated cells (BMNCs), which represent two common indicators used for the evaluation of radiation damages, showed a significant decrease after radiation, but recovered nearly healthy levels upon treatment with Fe@C or CoNi@C (Fig. 4(b) and Fig. S9 in the ESM). This effect was attributed to the repair of radiation damages achieved by ROS scavenging [34–36]. Vital hematological and biochemical indicators (Figs. S10(a) and S10(b) in the ESM) drastically decreased after irradiation, but gradually returned to healthy levels through the treatments [34–36].

To probe ROS accumulation in the organs, the SOD and 3,4-methylenedioxyamphetamine (MDA) levels in liver and lungs were measured 1, 8, and 14 days after Fe@C and CoNi@C treatments (Figs. 4(d)–4(g)). The SOD levels significantly dropped after irradiation, indicating radiation-induced ROS accumulation in liver and lungs. After treatments with Fe@C and CoNi@C, the SOD levels increased by an appreciable amount. Similar trends were observed for MDA in liver and lungs. *Ex vivo* intestinal tissue staining revealed high cell apoptotic levels in irradiated mice, with massive ROS production (Figs. 4(h)–4(k)). Such apoptosis could be efficiently limited by Fe@C and CoNi@C treatments, which led to sufficient recovery from radiation damage (Fig. 4(c)). Chromosome aberration and formation of micronuclei in irradiated cells were also largely prevented by Fe@C and CoNi@C treatments (Fig. S11 in the ESM). No significant systemic toxicities in mice were found up to 30 days (Figs. S12–S17 in the ESM), consistent with previous acute and chronic toxicological investigations [30, 37–39]. It is worth noting that Fe@C and CoNi@C show high liver uptake in Fig. S12 in the ESM, due to their large particle size and surface chemistry, which is not optimized [40]. Particles with hydrodynamic diameter smaller than 5.5 nm can be excreted via the kidneys, thus avoiding potential accumulation-induced toxicity [41]. This highlights the need of further work to design highly catalytic ultra-small clusters [42–44] or small molecules [45, 46] with rapid renal clearance, which can further improve the biocompatibility and pharmacokinetics of these systems, of great importance for their clinical applications. Moreover, the integration of electrocatalytic processes and rational material design could represent a universal strategy for developing other biomaterials besides radioprotectants, such as antioxidants and antiaging [47–49], radiotherapy [43, 50–53], and chemotherapy [54, 55] agents.

3 Conclusions

In summary, we synthesized highly active Fe@C and CoNi@C radioprotective nanomaterials and investigated the corresponding biocatalytic and radiation protection processes *in vitro* and *in vivo*. Electrochemical characterizations and DFT calculations showed that the M@C nanomaterials have strong catalytic activity toward O_2, H_2O_2, and O_3 and can efficiently convert oxygen free radicals (·OH, $\cdot O_2^-$, and $HO_2\cdot$) into O_2 and H_2O, further confirmed by irradiation experiments on mice. The synthesized nanoshields can considerably reduce the amount of radiation-induced oxygen free radicals in cells and prevent DNA damage. *In vivo* radiation protection experiments showed a considerable improvement in the survival rate of irradiated mice, which increased to 90%. Evaluation of SOD and MDA levels showed that the present nanomaterials lead to increased SOD levels and decrease the harmful MDA content via scavenging of oxygen free radicals. Long-term monitoring showed that the present highly catalytically active nanoshields can repair radiation damage in the peripheral blood system while exhibiting minimal toxicities over 30 days.

4 Experimental

4.1 Materials synthesis

M@Cs samples were prepared according to the procedure described in our previous work [22]. In a typical experiment, first, 3.6 mmol of metal-containing precursors, i.e., $Fe(NO_3)_3{\cdot}9H_2O$ or a 1:1 (molar ratio) mixture of $Co(NO_3)_2{\cdot}6H_2O$ and $Ni(NO_3)_2{\cdot}6H_2O$, was filled into the channels of SBA-15 (1.0 g) by an

impregnation method. Then, the catalysts were placed into a chemical vapor deposition (CVD) furnace and the temperature was programmed to increase from 30 to 700 ˚C under a H_2 atmosphere, followed by bubbling CH_3CN at 700 ˚C. Finally, the samples were treated in a 4% HF aqueous solution at room temperature for 8 h, washed in distilled water and ethanol, and dried in an oven at 100 ˚C for 12 h. The samples obtained from $Fe(NO_3)_3{\cdot}9H_2O$ or $Co(NO_3)_2{\cdot}6H_2O$/$Ni(NO_3)_2{\cdot}6H_2O$ precursors were denoted as Fe@C and CoNi@C, respectively. The other M@Cs samples were prepared in the same way and denoted as Co@C, Ni@C, FeCo@C, and FeNi@C, according to the types of metal precursors employed.

4.2 Materials characterization

HRTEM was conducted on FEI Tecnai F30 and F20 microscopes operated at an accelerating voltage of 300 and 200 kV, respectively.

4.3 Electrochemical measurements

Electrochemical measurements were performed on a Princeton Applied Research potentiostat/galvanostat in a three-electrode electrochemical cell equipped with a gas flow controlling system. A commercial GCE (5 mm diameter, 0.196 cm^2 geometric surface area) modified with the sample and Nafion ionomer binder, a Pt wire, and a saturated calomel electrode (SCE) were used as the working, counter, and reference electrodes, respectively. Typically, 5 mg catalyst was ultrasonically dispersed in 2 mL ethanol with 50 μL Nafion solution (5 wt.%, Du Pont) to form a homogeneous ink. Then, 25 μL of the ink was added dropwise and uniformly onto the surface of the GCE using a micropipette and dried at room temperature. The final loading amount for all catalysts on the working electrode was 0.32 $mg{\cdot}cm^{-2}$. The electrocatalytic activities were evaluated by RDE measurements with a rotating speed of 2,500 rpm at 25 ˚C and a scan rate of 5 $mV{\cdot}s^{-1}$. The CV curves of the samples were obtained in the presence of Ar, O_2, 10.0 mM H_2O_2, and O_3 at the scan rate of 50 $mV{\cdot}s^{-1}$.

4.4 Computational details

The Vienna *ab-initio* simulation package (VASP) was used for the quantum chemical calculations, using the projector-augmented wave (PAW) method [56, 57]. All quantum chemical calculations were based on the generalized gradient approximation method and the Perdew–Burke–Ernzerhof (PBE) functional for the exchange-correlation energy [58]. Structural optimizations were performed with a cut-off energy of 400 eV and a (2 × 2 × 1) Monkhorst-Pack *k*-point grid was used to sample the Brillouin zone [59]. All structures were fully relaxed and spin polarization was included in all calculations. The convergence of energy and forces were set to 1×10^{-5} eV and 0.05 $eV{\cdot}Å^{-1}$, respectively.

Owing to the small curvature of the graphene layers in all experimental samples, the graphene-encapsulated metallic nanoparticles were modeled as flat single-layer graphene with attached metal clusters (Fe, Co, and Ni metal atoms and their alloys), as shown in Fig. 2. A unit cell of (12.8 × 12.3) Å and a vacuum space of ~ 20 Å were used. The binding energies of the reactive species adsorbed on the cluster surface were calculated as $\Delta E_{ad} = E_{total} - E_{surface} - \mu$, where E_{total} represents the total energy of the surface with the adsorbed species, $E_{surface}$ is the total energy of the catalyst surface alone, and μ is the chemical potential of the adsorbed species.

4.5 Cellular toxicity

CHO cells were employed for all *in vitro* investigations. A total of 4×10^3 cells in Dulbecco's modified Eagle medium (DMEM) (10% FBS) were seeded in a 96-well plate. After incubation for 24 h to reach sufficient confluence, the cells were treated with Fe@C and CoNi@C (at doses of 0.3, 1, 3, 9, and 27 $\mu g{\cdot}mL^{-1}$) in DMEM and in fresh medium for the control group. The toxicity was analyzed by NR assay after incubation for 24 and 48 h. Briefly, after discarding the old medium and adding 100 μL neutral red solution (4 mg NR dye, 1 mL H_2O, 79 mL DMEM) into each well, the 96-well plates were placed back in the cell incubator (37 ˚C, 5% CO_2) for 3 h. Then, the neutral red solution was removed, and each well was washed three times with PBS. A 150 μL volume of neutral red desorbing solution (glacial acid solution: ethanol:H_2O = 1:50:49) was added into each well and shaken for 10 min to

dissolve the NR inside the cells. The absorption at 540 nm was then recorded.

4.6 Cellular SOD and GSH levels

CHO-K1 and H460 cells were plated into six-well plates with 3×10^5 cells per well. Approximately 24 h later, two doses of Fe@C and CoNi@C solution (1 and 10 μg·mL^{-1}) were added into the wells and the plates were incubated for another 48 h. The cells were then washed with PBS and collected, prior to SOD and GSH testing. For the SOD assay, cells were homogenized using an ultrasonic processor operating at 100 W for 3 s each time, with 2 s intervals. The samples were then centrifuged at 6,000 rpm and 4 ℃ for 8 min, and the supernatants collected. The SOD levels were tested using a total superoxide dismutase assay kit with nitroblue tetrazolium (NBT) (S0109, Beyotime). Generally, 20 μL supernatant was added into a 1.5 mL Eppendorf (EP) tube, while 20 and 40 μL phosphate buffers were used as control 1 and control 2, respectively. A xanthine oxidase working solution (xanthine oxidase:NBT:PBS = 1:1:158) was added to each tube (160 μL). After thorough vortexing, 20 μL xanthine was added into each tube except control 2. All tubes were maintained at 37 ℃ and kept incubating for 30 min. Then, the complex solution was transferred into 96-well plates and analyzed using a microplate reader at 560 nm. The SOD activity was calculated as $[(A_{\text{control 1}} - A_{\text{sample}})/(A_{\text{control 1}} - A_{\text{control 2}})] \times 100\%$ ("A" stands for optical absorbance value).

For the GSH assay, after collecting cells by centrifugation, protein removal reagent M was added in an amount corresponding to three times the weight of the cell sediments. All cell samples were rapidly frozen by liquid nitrogen and thawed in a 37 ℃ water bath, and the process was repeated twice. The cell samples were placed in ice for 5 min and then centrifuged at 8,000 rpm for 10 min; the supernatants were collected for GSH testing in 96-well plates. Ten microliters of supernatant was added into a 96-well plate (using 10 μL protein removal reagent M as control), followed by the addition of 150 μL of GSH-testing working solution (6.6 μL glutathione reductase, 6.6 μL 5,5'-Dithiobis-(2-nitrobenzoic acid) (DTNB), 137 μL phosphate buffer). The samples were maintained at room temperature (25 ℃) after sufficient vortexing. Then, 0.5 mg·mL^{-1} nicotinamide adenine dinucleotide phosphate (NADPH) solution was rapidly added into each well with thorough mixing. The system was allowed to react for 25 min and then tested by a microplate reader at 412 nm. The amount of GSH in the samples was quantified by a standard curve obtained using glutathione disulfide (GSSG, 10, 5, 2, 1, and 0.5 μM).

4.7 Cellular localization and uptake

CHO-K1 cells were seeded in six-well plates (~ 10^5 cells per well) and incubated at 37 ℃ with 5% CO_2 for 24 h. Fe@C and CoNi@C nanoparticles were dissolved in ethanol as stock solution and kept in an ultrasound bath for 30 min. The concentration of all stock solutions was 4 mg·mL^{-1}. Then, the solution was diluted with DMEM (10% FBS) to reach the final dose of 30 μg·mL^{-1}. After cell adherence, Fe@C and CoNi@C solutions (30 μg·mL^{-1}) were placed into six-well plates 33, 25, 10, and 5 h before microscopic examination. All wells were washed with PBS three times. Bright field images were captured using an AMG microscope. Approximately 4×10^3 cells were grown in 96-well plates and incubated for 24 h, with six duplicates for each group. Fe@C and CoNi@C (30 μg·mL^{-1}) solutions were added into the wells 33, 30, 25, 22, 10, and 5 h before measuring the optical density (OD) values at 490 nm on a microplate reader, including six blank wells (without cells or culture media) as the initial amount. After incubation, all cell-seeded wells were washed with PBS to remove the residual unbound Fe@C and CoNi@C nanoparticles. The amount of uptake was calculated as the ratio between the OD value of M@C-treated wells and the average OD value of wells only containing M@Cs.

4.8 Colony assay

Three cell lines (CHO-K1, Hela, and H460) were seeded in six-well plates with 800 cells per well and incubated for 24 h. Fe@C and CoNi@C solutions (1 μg·mL^{-1}) were added 30 min before irradiation with 0, 2, 4, 6, and 8 Gy gamma rays. The cells were cultured for about 10 days and then fixed with methanol. Colony units were identified by Giemsa staining, and those with ≥ 50 cells were classified as survivors. The surviving fraction was calculated as the ratio between the plating efficiency of the treated

groups and that of the control groups. The obtained results were fitted to a single-hit, multitarget model.

4.9 Cell survival

A total of 3×10^3 cells were seeded into 96-well plates, and after reaching confluence, they were treated with Fe@C and CoNi@C (at a concentration of 1 μg·mL^{-1}) or fresh medium, 30 min before irradiation. Then, the cells were exposed to 3 Gy gamma radiation and further incubated for 48 h. Living cells were determined by NR assay, as described above. Hela and H460 cells were grown in 96-well plates with 4×10^3 cells per well. After 24 h incubation, the cells were treated with 0.3 μg·mL^{-1} Fe@C and CoNi@C solutions. After 30 min of incubation, the cells were exposed to 4 Gy gamma radiation, and then kept in the incubator for 48 h. Cell survival was measured by NR assay, as discussed above.

4.10 Intracellular ROS measurements

Six-well plates were seeded with 1×10^4 cells per well. After 24 h, the cells were treated with Fe@C and CoNi@C (0.3 μg·mL^{-1}) for 30 min before exposure to 3 Gy gamma radiation, and cultured for another 24 h. After removing the medium, 1 mL of 5 μM 2,7-dichlorodihydrofluorescein diacetate (DCFH-DA) was incubated for 20 min, followed by washing with PBS three times. The cells were then collected and the fluorescence intensity was measured by a BD (Becton, Dickinson) flow cytometer with an excitation wavelength of 488 nm and a wide-field fluorescence microscope (EVOS, AMG, USA).

4.11 Comet assay

Agarose (0.8%, 500 μL) was spread homogeneously on glass slides. The slides were allowed to solidify at 4 ˚C for 5 min, and 3×10^4 cells in 30 μL PBS were mixed with 70 μL low-melting point agarose (0.6%). Twenty microliters of the mixture was uniformly spread over the slides, which were then placed into cold fresh lysis buffer (2.5 mol·L^{-1} NaCl, 100 mmol·L^{-1} Na_2EDTA, 10 mmol·L^{-1} Tris-HCl, 10% DMSO, 1% Triton X-100) for 2.5 h and transferred into a horizontal gel electrophoresis unit (20 cm × 25 cm) filled with chilled electrophoresis buffer (1 mmol·L^{-1} Na_2EDTA, 300 mmol·L^{-1} NaOH, pH 7.5) for 30 min. The electrophoresis voltage was set to 30 V for 20 min. The slides were neutralized with Tris-HCl (0.06 g·mL^{-1}, pH 7.5) and stained with ethidium bromide (2 μg·mL^{-1}) for 1 min. The tail DNA and tail moment analyses were performed using 100 cells per group. About 20 images were taken for each group, and those showing a uniform cell distribution were selected for DNA damage evaluation. Outliers were excluded to ensure that the total number of cells in each group was 100. DNA damage was evaluated with the Comet Assay Software Project (CASP), which was used for the quantification of tail moment and total tail DNA.

4.12 Immunofluorescence assay

C57BL/6 mice were divided into four groups of six and then treated with distilled water, radiation, and Fe@C and CoNi@C at a dose of 2 mg·mL^{-1} (0.2 mL) before irradiation. The mice were injected with chloral hydrate (3.5%), in doses calculated as 1% of the body weight. After total anesthesia, the mice were laid flat and exposed to 13 Gy abdominal radiation with a dose rate of 0.98 Gy·min^{-1}. Small intestines were collected after 6 h of irradiation and fixed in 10% neutral buffered formalin for 48 h. The intestines were then embedded in paraffin and sectioned into slices on glass slides. All slides were dried at 37 ˚C for 1 h to completely remove water and washed in dimethylbenzene twice (15 min each time) to remove the paraffin. Subsequently, the slides were immersed in sequence in 100%, 90%, and 70% ethanol for 10 min. Afterward, the slides were further washed with distilled water for 5 min. A TdT-mediated dUTP Nick-End Labeling (TUNEL) kit (Beyotime, C1090) was employed to analyze the apoptosis of intestine cells after irradiation. The slides were incubated with Proteinase K (20 μg·mL^{-1}) at 37 ˚C for 15 min and then washed with PBS three times. A TUNEL testing solution (Terminal Deoxynucleotidyl Transferase (TdT):Cy3 = 1:24) was added onto the slides and placed at 37 ˚C for 60 min. After washing three times with PBS, 6-diamidino-2-phenylindole (DAPI) staining was used to localize the nuclei. The slides were mounted with anti-fade mounting medium and analyzed by fluorescent microscopy at excitation/emission wavelengths of 340/488 nm for DAPI and 550/570 nm for Cy3.

Eighteen C57 mice were randomly divided into three groups: Fe@C-treated, CoNi@C-treated, and control group. The mice were intravenously injected with Fe@C and CoNi@C solution (2 mg·mL^{-1}) and fed for 30 days. Livers and lungs were then collected from each mouse, fixed in 10% formalin for 48 h, and embedded into paraffin. The tissue slices were stained using the TUNEL kit mentioned above.

4.13 Chromosomal aberration assay

Peripheral blood was drawn from healthy human adults and put in 5 mL EP tubes. The blood samples were treated with Fe@C and CoNi@C at the final dose of 0.3 μg·mL^{-1}. After 30 min, the blood samples were exposed to 3 Gy gamma radiation, placed into a cell incubator at 37 °C supplemented with CO_2 for 2 h, and then transferred into a chromosome culture medium. After 51 h of irradiation, demecolcine (25 μg·mL^{-1}) was introduced in the culture medium at 37 °C for 1 h. Blood cells were collected by centrifugation for 5 min at 1,000 rpm. KCl (0.075 M) was added for 30 min and replaced by 0.5 mL Carnoy's fluid (CH_3OH:CH_3COOH = 3:1). After collecting the blood cells by centrifugation (1,200 rpm, 8 min), the supernatant was discarded and 8 mL of Carnoy's fluid was added twice (30 min each time) for fixing the cells. After centrifugation, cells were placed dropwise onto glass slides, which were then dried at 50 °C and stained with Giemsa dye. The samples were analyzed by optical microscopy.

4.14 Micronucleus assay

Peripheral blood was drawn from healthy human adults and put in 5 mL EP tubes. The blood samples were treated with Fe@C and CoNi@C at the final dose of 0.3 μg·mL^{-1}. After 30 min, the blood samples were exposed to 3 Gy gamma radiation and placed for 2 h into a cell incubator at 37 °C supplemented with CO_2, and then transferred into chromosome culture medium. After 72 h, the medium was removed and 6 mL 0.1 M KCI was added, followed by the addition of 0.6 mL of Carnoy's fluid. Lymphocytes were collected by centrifugation at 1,200 rpm for 8 min. Carnoy's fluid (6 mL) was added to fix cells twice, for 30 min each time. The samples were gently spread over glass slides, dried at room temperature, stained with Giemsa dye, and finally analyzed by an optical microscope.

4.15 *In vivo* radiation protection tests

The male C57BL/6 mice used in this study were approved by the Institutional Animal Care and Use Committee (IACUC), and handled under protocols approved by the Institute of Radiation Medicine, Chinese Academy of Medical Sciences (IRM, CAMS). The mice were divided into different groups (with 10 animals in each group): besides the control group, the other groups comprised mice exposed to radiation after injection of distilled water, amifostine, graphene, graphite, and M@Cs (M = Fe, Ni, Co, FeCo, FeNi, CoNi) at a dose of 20 mg·kg^{-1} (0.2 mL, 2 mg·mL^{-1}). After a 30 min injection, mice were exposed to 7.5 Gy whole-body gamma radiation using ^{137}Cs (662 keV, 3600 Ci). The survival rates were monitored on a daily basis.

4.16 Hematology and biochemistry panels

Seventy-two C57BL/6 mice were divided into nine groups: mice exposed to radiation only, and mice exposed to radiation after treatment with Fe@C or CoNi@C prior to sacrifice on day 1, 8, and 14. The mice were treated with distilled water, Fe@C, or CoNi@C, and then received 7 Gy whole-body radiation. Mice were sacrificed after 1, 8, and 14 days, and a saphenous blood collection technique was used to draw samples of specific blood cells (about 1 mL) and dilute them from 20 to 1,000 μL. The hematological parameters were evaluated with a cytometer (Mindray, 2800BC-Vet). The remaining blood samples were placed at 4 °C overnight and centrifuged at 6,000 rpm for 5 min to obtain serum for the biochemistry analysis.

4.17 SOD and MDA levels

Mice were divided into the following groups (with six mice per group): control, mice exposed to radiation only, and mice exposed to radiation and then treated with Fe@C or CoNi@C; each group was further divided into subgroups corresponding to day 1, 8, and 14. Mice in the control and radiation-only groups were administered 200 μL distilled water, whereas those in the treated groups were injected 200 μL

Fe@C or CoNi@C solution (2 mg·mL^{-1}). With the exception of the control group, the whole body of every mouse in the other groups was irradiated with 7 Gy gamma rays. After 1, 8, and 14 days of treatment, the mice were sacrificed to collect livers and lungs. The apexes of the livers (about 0.2 g) were cut off and placed in 10 mL centrifuge tubes, whereas lungs were harvested as a whole. All organs were immersed in a saline solution of volume 10 times that of the organ. Organ samples were homogenized by a tissue homogenate machine (IKA, T18 Basic) to yield 10% tissue homogenates, which were placed in ice for 2 h and centrifuged at 3,500 rpm for 8 min. The resulting solution was diluted into 1% and 0.25% homogenates. For measuring the total SOD levels, 1 mL of 7.5 mM phosphate buffer was added into 5 mL EP tubes and mixed with 50 μL 0.25% liver or lung homogenates or 50 μL distilled water as control. Hydroxylamine hydrochloride (0.1 M, 100 μL), xanthine (75 mM, 100 μL), and xanthine oxidase (0.037 U·L^{-1}, 100 μL) solutions were added into the samples in that sequence, fully mixed, and incubated at 37 ℃ for 40 min. Subsequently, 2 mL nitrite developer ($C_{10}H_9N$: $C_6H_7NO_3S$: CH_3COOH = 3:3:2) was added into the system. The optical absorption at 550 nm was recorded with an ultraviolet–visible (UV–vis) spectrophotometer UV-1750, (Shimadzu, Japan). The MDA analysis was carried out using tissue homogenates (10%). Identical volumes (100 μL) of the tested sample, ethanol, and tetraethoxypropane (10 nmol·mL^{-1}) were individually added into 5 mL EP tubes. Ethanol and tetraethoxypropane were used as negative and positive controls, respectively. Tissue lysis solution (100 μL) was added into each 5 mL-EP tube and thoroughly mixed. Trichloroacetic acid (10%, 3 mL) and thiobarbituric acid (0.6%, H_2O:CH_3COOH = 1:1, 1 mL) were added to the system in that sequence. Then, the tubes were boiled in 95 ℃ water for 40 min. All samples were centrifuged at 3,500–4,000 rpm for 10 min after being cooled down to room temperature. The 532-nm absorption of the supernatants was measured by a UV–vis spectrophotometer.

4.18 Measurement of bone marrow total DNA and nucleated cells

To measure the bone marrow total DNA, the bilateral femurs of each mouse were excised from the body with connective tissues completely removed. Bone marrow cells were flushed from the femur with 10 mL 0.005 M calcium chloride solution using a 24-gauge needle to obtain single cell suspensions. The suspensions were kept at 4 ℃ for 30 min and centrifuged at 2,500 rpm for 15 min, with the supernatants discarded. The sediments were mixed with perchloric acid (5 mL, 0.2 M) and placed in a water bath heated at 90 ℃ for 15 min. Subsequently, the mixture solutions were allowed to cool naturally to room temperature and purified through filters, and the UV absorption at 268 nm of the filtrates was measured with an ultraviolet spectrophotometer. To count the number of bone marrow nucleated cells, the bone marrow cells were flushed with 1 mL PBS and filtered through a 200-mesh nylon filter for removing fragments of bone and tissue, before the cytometric analysis (Mindray, BC-2800 Vet).

4.19 *In vivo* toxicity assay

C57BL/6 mice were divided in a control group and groups comprising mice treated with Fe@C or CoNi@C (eight mice for each group) on day 1, 7, and 30. The mice were injected intraperitoneally with 200 μL distilled water, Fe@C, or CoNi@C (at a dose of 2 mg·mL^{-1}). All mice were weighed every other day. Immune responses were evaluated by collecting spleens and thymus on day 1, 7, and 30 and calculating the organ index as the ratio of organ weight (mg) to body weight (g). The mice were sacrificed on day 1, 7, and 30 using isoflurane and anesthetic angiocatheter exsanguinations. Blood samples were acquired by a standard saphenous blood collection technique and part of the drawn blood (20 μL) was placed into potassium ethylenediaminetetraacetic acid (EDTA) collection tubes for hematological analysis. The remaining blood was kept at 4 ℃ overnight and centrifuged at 6,000 rpm for 5 min to separate serum for biochemical evaluation. Meanwhile, major organs (heart, liver, spleen, lung, and kidney) were harvested, fixed in 10% neutral buffered formalin, processed by embedding in paraffin, and stained with hematoxylin and eosin (H&E). The pathology was analyzed using a digital microscope.

4.20 Tissue SOD and GSH levels

C57 mice were randomly divided into three groups: control group, mice treated with Fe@C, and mice treated with CoNi@C (six mice for each group). The mice were intravenously injected with Fe@C or CoNi@C solution at the concentration of 2 mg·mL^{-1} and raised for 30 days. Livers and lungs were collected from each mouse and homogenized in PBS for the SOD assay and protein removal reagent M for the GSH assay, to obtain 10% tissue homogenates. The remaining procedures were carried out according to the instructions of the Beyotime testing kits, as mentioned above.

4.21 Biodistribution

C57BL/6 mice were divided into the following groups (six animals in each group): control mice and mice treated with Fe@C or CoNi@C for 1, 7, and 30 days. The mice were treated with distilled water, Fe@C, or CoNi@C (2 mg·mL^{-1}, 0.2 mL) and sacrificed on day 1, 7, and 30. The heart, liver, spleen, lung, kidney and testis of each mouse were collected for inductively coupled plasma-mass spectrometry (ICP-MS) analyses. A 0.5 g amount of each organ was weighed and digested in 6 mL nitric acid in a microwave device (Mars 5, CEM, Kamp Lintfort, Germany). After condensing the samples to 1–2 mL in an electric heater, the solution was transferred into polyethylene terephthalate bottles with weight adjusted to 50.00 g using 2% nitric acid. The concentrations of Fe, Co, and Ni were determined by ICP-MS (Agilent, 7500 CE, Agilent Technologies, Waldbronn, Germany).

4.22 Statistical analysis

All data obtained in this study are presented as mean ± standard deviation (SD). The independent Student's *t*-test was used for the statistical analysis.

Acknowledgements

We gratefully acknowledge the financial support from the Ministry of Science and Technology of China (Nos. 2016YFA0204100 and 2016YFA0200200), the National Natural Science Foundation of China (Nos. 81471786, 21573220, and 21303191), the strategic Priority Research Program of the Chinese Academy of Sciences (No. XDA09030100), Natural Science Foundation of Tianjin (No. 13JCQNJC13500). We also acknowledge the Shanghai Supercomputer Center for the computational resources. The authors would like to thank Dr. Guosong Hong (Harvard University) for some helpful discussions.

Electronic Supplementary Material: Supplementary material (Figs. S1–S17 and Table S1) is available in the online version of this article at https://doi.org/10.1007/s12274-017-1912-9.

References

[1] Lushbaugh, C. C.; Casarett, G. W. The effects of gonadal irradiation in clinical radiation therapy: A review. *Cancer* **1976**, *37*, 1111–1120.

[2] Laperriere, N.; Zuraw, L.; Cairncross, G. Radiotherapy for newly diagnosed malignant glioma in adults: A systematic review. *Radiother. Oncol.* **2002**, *64*, 259–273.

[3] Bentzen, S. M. Preventing or reducing late side effects of radiation therapy: Radiobiology meets molecular pathology. *Nat. Rev. Cancer* **2006**, *6*, 702–713.

[4] Evans, H. J.; Buckton, K. E.; Hamilton, G. E.; Carothers, A. Radiation-induced chromosome aberrations in nuclear-dockyard workers. *Nature* **1979**, *277*, 531–534.

[5] Hainfeld, J. F.; Dilmanian, F. A.; Slatkin D. N.; Smilowitz, H. M. Radiotherapy enhancement with gold nanoparticles. *J. Pharm. Pharmacol.* **2008**, 60, 977–985.

[6] Chandra, J.; Samali, A.; Orrenius, S. Triggering and modulation of apoptosis by oxidative stress. *Free Radic. Biol. Med.* **2000**, *29*, 323–333.

[7] Mishra, K. P. Cell membrane oxidative damage induced by gamma-radiation and apoptotic sensitivity. *J. Environ. Pathol. Toxicol. Oncol.* **2004**, *23*, 61–66.

[8] Yuan, X.; Setyawati, M. I.; Leong, D. T.; Xie, J. P. Ultrasmall Ag^{+}-rich nanoclusters as highly efficient nanoreservoirs for bacterial killing. *Nano Res.* **2014**, *7*, 301–307.

[9] Talmage, D. W. Effect of ionizing radiation on resistance and infection. *Annu. Rev. Microbiol.* **1955**, *9*, 335–346.

[10] Colon, J.; Herrera, L.; Smith, J.; Patil, S.; Komanski, C.; Kupelian, P.; Seal, S.; Jenkins, D. W.; Baker, C. H. Protection from radiation-induced pneumonitis using cerium oxide nanoparticles. *Nanomed.-Nanotechnol. Biol. Med.* **2009**, *5*, 225–231.

[11] Fan, S.; Meng, Q.; Xu, J.; Jiao, Y.; Zhao, L.; Zhang, X.; Sarkar, F. H.; Brown, M. L.; Dritschilo, A.; Rosen, E. M. DIM (3, 3′-diindolylmethane) confers protection against ionizing radiation

by a unique mechanism. *Proc. Natl. Acad. Sci. USA* **2013**, *110*, 18650–18655.

[12] Zhang, X.-D.; Zhang, J. X.; Wang, J. Y.; Yang, J.; Chen, J.; Shen, X.; Deng, J.; Deng, D. H.; Long, W.; Sun, Y.-M. et al. Highly catalytic nanodots with renal clearance for radiation protection. *ACS Nano* **2016**, *10*, 4511–4519.

[13] Tarnuzzer, R. W.; Colon, J.; Patil, S.; Seal, S. Vacancy engineered ceria nanostructures for protection from radiation-induced cellular damage. *Nano Lett.* **2005**, *5*, 2573–2577.

[14] Li, Y. Y.; He, X.; Yin, J. J.; Ma, Y. H.; Zhang, P.; Li, J. Y.; Ding, Y. Y.; Zhang, J.; Zhao, Y. L.; Chai, Z. F. et al. Acquired superoxide-scavenging ability of ceria nanoparticles. *Angew. Chem., Int. Ed.* **2015**, *54*, 1832–1835.

[15] Feliciano, C. P.; Tsuboi, K.; Suzuki, K.; Kimura, H.; Nagasaki, Y. Long-term bioavailability of redox nanoparticles effectively reduces organ dysfunctions and death in whole-body irradiated mice. *Biomaterials* **2017**, *129*, 68–82.

[16] Pacelli, C.; Bryan, R. A.; Onofri, S.; Selbmann, L.; Shuryak, I.; Dadachova, E. Melanin is effective in protecting fast and slow growing fungi from various types of ionizing radiation. *Environ. Microbiol.* **2017**, *19*, 1612–1624.

[17] Briggs, A.; Corde, S.; Oktaria, S.; Brown, R.; Rosenfeld, A.; Lerch, M.; Konstantinov, K.; Tehei, M. Cerium oxide nanoparticles: Influence of the high-Z component revealed on radioresistant 9L cell survival under X-ray irradiation. *Nanomed.-Nanotechnol. Biol. Med.* **2013**, *9*, 1098–1105.

[18] Colon, J.; Hsieh, N.; Ferguson, A.; Kupelian, P.; Seal, S.; Jenkins, D. W.; Baker, C. H. Cerium oxide nanoparticles protect gastrointestinal epithelium from radiation-induced damage by reduction of reactive oxygen species and upregulation of superoxide dismutase 2. *Nanomed.-Nanotechnol. Biol. Med.* **2010**, *6*, 698–705.

[19] Che, P.; Liu, W.; Chang, X. X.; Wang, A. H.; Han, Y. S. Multifunctional silver film with superhydrophobic and antibacterial properties. *Nano Res.* **2016**, *9*, 442–450.

[20] Kang, D.-W.; Kim, C. K.; Jeong, H.-G.; Soh, M.; Kim, T.; Choi, I.-Y.; Ki, S.-K.; Yang, W.; Hyeon, T.; Lee, S.-H. Biocompatible custom ceria nanoparticles against reactive oxygen species resolve acute inflammatory reaction after intracerebral hemorrhage. *Nano Res.* **2017**, *10*, 2743–2760.

[21] Deng, D. H.; Yu, L.; Chen, X. Q.; Wang, G. X.; Jin, L.; Pan, X. L.; Deng, J.; Sun, G. Q.; Bao, X. H. Iron encapsulated within pod-like carbon nanotubes for oxygen reduction reaction. *Angew. Chem., Int. Ed.* **2013**, *52*, 371–375.

[22] Cui, X. J.; Ren, P. J.; Deng, D. H.; Deng, J.; Bao, X. H. Single layer graphene encapsulating non-precious metals as high-performance electrocatalysts for water oxidation. *Energy Environ. Sci.* **2016**, *9*, 123–129.

[23] Deng, D. H.; Novoselov, K. S.; Fu, Q.; Zheng, N. F.; Tian, Z. Q.; Bao, X. H. Catalysis with two-dimensional materials and their heterostructures. *Nat. Nanotechnol.* **2016**, *11*, 218–230.

[24] Gong, M.; Wang, D.-Y.; Chen, C.-C.; Hwang, B.-J.; Dai, H. J. A mini review on nickel-based electrocatalysts for alkaline hydrogen evolution reaction. *Nano Res.* **2016**, *9*, 28–46.

[25] Gong, M.; Dai, H. J. A mini review of NiFe-based materials as highly active oxygen evolution reaction electrocatalysts. *Nano Res.* **2015**, *8*, 23–39.

[26] Nørskov, J. K.; Rossmeisl, J.; Logadottir, A.; Lindqvist, L.; Kitchin, J. R.; Bligaard, T.; Jónsson, H. Origin of the overpotential for oxygen reduction at a fuel-cell cathode. *J. Phys. Chem. B* **2004**, *108*, 17886–17892.

[27] Rossmeisl, J.; Karlberg, G. S.; Jaramillo, T.; Nørskov, J. K. Steady state oxygen reduction and cyclic voltammetry. *Faraday Discuss.* **2008**, *140*, 337–346.

[28] Rossmeisl, J.; Qu, Z. W.; Zhu, H.; Kroes, G. J.; Nørskov, J. K. Electrolysis of water on oxide surfaces. *J. Electroanal. Chem.* **2007**, *607*, 83–89.

[29] Yang, K.; Li, Y. J.; Tan, X. F.; Peng, R.; Liu, Z. Behavior and toxicity of graphene and its functionalized derivatives in biological systems. *Small* **2013**, *9*, 1492–1503.

[30] Yang, K.; Zhang, S.; Zhang, G. X.; Sun, X. M.; Lee, S.-T.; Liu, Z. Graphene in mice: Ultrahigh *in vivo* tumor uptake and efficient photothermal therapy. *Nano Lett.* **2010**, *10*, 3318–3323.

[31] Sun, X. M.; Liu, Z.; Welsher, K.; Robinson, J. T.; Goodwin, A.; Zaric, S.; Dai, H. Nano-graphene oxide for cellular imaging and drug delivery. *Nano Res.* **2008**, *1*, 203–212.

[32] Liu, Z.; Tabakman, S.; Welsher, K.; Dai, H. J. Carbon nanotubes in biology and medicine: *In vitro* and *in vivo* detection, imaging and drug delivery. *Nano Res.* **2009**, *2*, 85–120.

[33] Yu, C. Y. Y.; Xu, H. E.; Ji, S. L.; Kwok, R. T. K.; Lam, J. W. Y.; Li, X. L.; Krishnan, S.; Ding, D.; Tang, B. Z. Mitochondrion-anchoring photosensitizer with aggregation-induced emission characteristics synergistically boosts the radiosensitivity of cancer cells to ionizing radiation. *Adv. Mater.* **2017**, *29*, 1606167.

[34] Zhang, X. D.; Chen, J.; Min, Y. H.; Park, G. B.; Shen, X.; Song, S. S.; Sun, Y. M.; Wang, H.; Long, W.; Xie, J. et al. Metabolizable Bi_2Se_3 nanoplates: Biodistribution, toxicity, and uses for cancer radiation therapy and imaging. *Adv. Funct. Mater.* **2014**, *24*, 1718–1729.

[35] Zhang, X. D.; Chen, J.; Luo, Z. T.; Wu, D.; Shen, X.; Song, S. S.; Sun, Y. M.; Liu, P. X.; Zhao, J.; Huo, S. D. et al. Enhanced tumor accumulation of sub-2 nm gold nanoclusters for cancer radiation therapy. *Adv. Healthcare Mater.* **2014**, *3*, 133–141.

[36] Hauck, T. S.; Anderson, R. E.; Fischer, H. C.; Newbigging, S.; Chan, W. C. W. *In vivo* quantum-dot toxicity assessment. *Small* **2010**, *6*, 138–144.

[37] Liu, Z.; Davis, C.; Cai, W.; He, L.; Chen, X.; Dai, H. Circulation and long-term fate of functionalized, biocompatible single-walled carbon nanotubes in mice probed by Raman spectroscopy. *Proc. Natl. Acad. Sci. USA* **2008**, *105*, 1410–1415.

[38] Huang, X. L.; Zhang, F.; Zhu, L.; Choi, K. Y.; Guo, N.; Guo, J. X.; Tackett, K.; Anilkumar, P.; Liu, G.; Quan, Q. M. et al. Effect of injection routes on the biodistribution, clearance, and tumor uptake of carbon dots. *ACS Nano* **2013**, *7*, 5684–5693.

[39] Zhang, W. D.; Wang, C.; Li, Z. J.; Lu, Z. Z.; Li, Y. Y.; Yin, J. J.; Zhou, Y. T.; Gao, X. F.; Fang, Y.; Nie, G. J. et al. Unraveling stress-induced toxicity properties of graphene oxide and the underlying mechanism. *Adv. Mater.* **2012**, *24*, 5391–5397.

[40] Khlebtsov, N.; Dykman, L. Biodistribution and toxicity of engineered gold nanoparticles: A review of *in vitro* and *in vivo* studies. *Chem. Soc. Rev.* **2011**, *40*, 1647–1671.

[41] Choi, H. S.; Liu, W. H.; Misra, P.; Tanaka, E.; Zimmer, J. P.; Ipe, B. I.; Bawendi, M. G.; Frangioni, J. V. Renal clearance of quantum dots. *Nat. Biotechnol.* **2007**, *25*, 1165–1170.

[42] Liu, J. B.; Yu, M. X.; Zhou, C.; Yang, S. Y.; Ning, X. H.; Zheng, J. Passive tumor targeting of renal-clearable luminescent gold nanoparticles: Long tumor retention and fast normal tissue clearance. *J. Am. Chem. Soc.* **2013**, *135*, 4978–4981.

[43] Zhang, X. D.; Luo, Z. T.; Chen, J.; Shen, X.; Song, S. S.; Sun, Y. M.; Fan, S. J.; Fan, F. Y.; Leong, D. T.; Xie, J. P. Ultrasmall $Au_{10-12}(SG)_{10-12}$ nanomolecules for high tumor specificity and cancer radiotherapy. *Adv. Mater.* **2014**, *26*, 4565–4568.

[44] Liu, J.; Wang, P. Y.; Zhang, X.; Wang, L. M.; Wang, D. L.; Gu, Z. J.; Tang, J. L.; Guo, M. Y.; Cao, M. J.; Zhou, H. G. et al. Rapid degradation and high renal clearance of Cu_3BiS_3 nanodots for efficient cancer diagnosis and photothermal therapy *in vivo*. *ACS Nano* **2016**, *10*, 4587–4598.

[45] Zhang, X. D.; Wang, H. S.; Antaris, A. L.; Li, L. L.; Diao, S.; Ma, R.; Nguyen, A.; Hong, G. S.; Ma, Z. R.; Wang, J. et al. Traumatic brain injury imaging in the second near-infrared window with a molecular fluorophore. *Adv. Mater.* **2016**, *28*, 6872–6879.

[46] Feng, L. Z.; Cheng, L.; Dong, Z. L.; Tao, D. L.; Barnhart, T. E.; Cai, W. B.; Chen, M. W.; Liu, Z. Theranostic liposomes with hypoxia-activated prodrug to effectively destruct hypoxic tumors post-photodynamic therapy. *ACS Nano* **2016**, *11*, 927–937.

[47] Zhang, C.; Zhao, K. L.; Bu, W. B.; Ni, D. L.; Liu, Y. Y.; Feng, J. W.; Shi, J. L. Marriage of scintillator and semiconductor for synchronous radiotherapy and deep photodynamic therapy with diminished oxygen dependence. *Angew. Chem., Int. Ed.* **2015**, *127*, 1790–1794.

[48] Cong, W. S.; Wang, P.; Qu, Y.; Tang, J. L.; Bai, R.; Zhao, Y. L.; Chen, C. Y.; Bi, X. L. Evaluation of the influence of fullerenol on aging and stress resistance using *Caenorhabditis Elegans*. *Biomaterials* **2015**, *42*, 78–86.

[49] Zhang, W.; Hu, S. L.; Yin, J.-J.; He, W. W.; Lu, W.; Ma, M.; Gu, N.; Zhang, Y. Prussian blue nanoparticles as multienzyme mimetics and reactive oxygen species scavengers. *J. Am. Chem. Soc.* **2016**, *138*, 5860–5865.

[50] Song, G. S.; Liang, C.; Yi, X.; Zhao, Q.; Cheng, L.; Yang, K.; Liu, Z. Perfluorocarbon-loaded hollow Bi_2Se_3 nanoparticles for timely supply of oxygen under near-infrared light to enhance the radiotherapy of cancer. *Adv. Mater.* **2016**, *28*, 2716–2723.

[51] Nakayama, M.; Sasaki, R.; Mukohara, T.; Ogino, C.; Morita, K.; Umetsu, M.; Ohara, S.; Sato, K.; Numako, C.; Takami, S. et al. Abstract 3337: Titanium peroxide nanoparticles enhance anti-tumor efficacy through reactive oxygen species in pancreatic cancer radiation therapy. *Cancer Res.* **2015**, *75*, 3337.

[52] Shim, M. S.; Xia, Y. N. A reactive oxygen species (ROS)-responsive polymer for safe, efficient, and targeted gene delivery in cancer cells. *Angew. Chem., Int. Ed.* **2013**, *52*, 6926–6929.

[53] Yi, X.; Chen, L.; Zhong, X. Y.; Gao, R. L.; Qian, Y. T.; Wu, F.; Song, G. S.; Chai, Z. F.; Liu, Z.; Yang, K. Core–shell Au@MnO_2 nanoparticles for enhanced radiotherapy via improving the tumor oxygenation. *Nano Res.* **2016**, *9*, 3267–3278.

[54] Wang, L. M.; Sun, Q.; Wang, X.; Wen, T.; Yin, J.-J.; Wang, P. Y.; Bai, R.; Zhang, X.-Q.; Zhang, L.-H.; Lu, A.-H. et al. Using hollow carbon nanospheres as a light-induced free radical generator to overcome chemotherapy resistance. *J. Am. Chem. Soc.* **2015**, *137*, 1947–1955.

[55] Wang, L. M.; Zhang, T. L.; Li, P. Y.; Huang, W. X.; Tang, J. L.; Wang, P. Y.; Liu, J.; Yuan, Q. X.; Bai, R.; Li, B. et al. Use of synchrotron radiation-analytical techniques to reveal chemical origin of silver-nanoparticle cytotoxicity. *ACS Nano* **2015**, *9*, 6532–6547.

[56] Kresse, G.; Furthmüller, J. Efficient iterative schemes for *ab initio* total energy calculations using a plane-wave basis set. *Phys. Rev. B* **1996**, *54*, 11169–11186.

[57] Blöchl, P. E. Projector augmented-wave method. *Phys. Rev. B* **1994**, *50*, 17953–17979.

[58] Perdew, J. P.; Burke, K.; Ernzerhof, M. Generalized gradient approximation made simple. *Phys. Rev. Lett.* **1996**, *77*, 3865–3868.

[59] Monkhorst, H. J.; Pack, J. D. Special points for Brillouin-zone integrations. *Phys. Rev. B* **1976**, *13*, 5188–5192.